PCCP

PAPER

View Article Online
View Journal | View Issue

Cite this: *Phys. Chem. Chem. Phys.*, 2021, **23**, 7806

Inelastic helium atom scattering from Sb_2Te_3(111): phonon dispersion, focusing effects and surfing

Adrian Ruckhofer,[a] Simon Halbritter,[a] Henriette E. Lund,[b] Ann Julie U. Holt,[b] Marco Bianchi,[b] Martin Bremholm,[c] Giorgio Benedek,[de] Philip Hofmann,[b] Wolfgang E. Ernst[a] and Anton Tamtögl[a]

Received 8th September 2020,
Accepted 20th October 2020

DOI: 10.1039/d0cp04738d

rsc.li/pccp

We present an experimental study of inelastic scattering processes on the (111) surface of the topological insulator Sb_2Te_3 using helium atom scattering. In contrast to other binary topological insulators such as Bi_2Se_3 and Bi_2Te_3, Sb_2Te_3 is much less studied and the as-grown Sb_2Te_3 sample turns out to be p-doped, with the Fermi-level located below the Dirac-point as confirmed by angle-resolved photoemission spectroscopy. We report the surface phonon dispersion along both high symmetry directions in the energy region below 11 meV, where the Rayleigh mode exhibits the strongest intensity. The experimental data is compared with a study based on density functional perturbation theory calculations, providing good agreement except for a set of additional peculiar inelastic events below the Rayleigh mode. In addition, an analysis of angular scans with respect to a number of additional inelastic events is presented, including resonance enhancement, kinematical focusing, focused inelastic resonance and surfing. In the latter case, phonon-assisted adsorption of the incident helium atom gives rise to a bound state where the helium atom rides the created Rayleigh wave.

1 Introduction

Antimony telluride (Sb_2Te_3) is a prominent p-type semiconductor and multifunctional material, well known for its outstanding thermoelectric properties at room temperature[1] and is used in power generation, heat pumping, cooling applications and data storage.[2] Approaches to further improve thermoelectric efficiency in low dimensional systems[3–5] and the contribution of topological surface states to thermoelectric properties have been investigated by Hinsche *et al.*[6] and show a possible involvement to enhanced phonon scattering. Sb_2Te_3 also plays a major role in phase change memory alloys[7] and recently sparked great interest in the field of topological insulators (TIs).[8–10]

TIs are described as a new type of quantum material, where the band gap present in the bulk, is closed by topologically protected surface states, forming a single Dirac-cone at the $\bar{\Gamma}$-point. These states arise from the combination of spin–orbit interaction and time-reversal symmetry.[11–13] Besides the well investigated binary compounds Bi_2Se_3 and Bi_2Te_3, Sb_2Te_3 has been confirmed to be a three-dimensional TI with a single Dirac cone on the surface.[8,14–16]

The Fermi-level of as-grown p-doped Sb_2Te_3 is located below the Dirac-point and Sb_2Te_3 can exhibit hole pockets in the $\overline{\Gamma M}$ direction, depending on the position of the Fermi-level.[16] However, it has been shown that the surface Fermi level can be shifted above the Dirac point, without changing the band structure, by n-doping with Cs.[17] While the surface electronic states of Sb_2Te_3(111) have been investigated, by angle-resolved photoemission spectroscopy (ARPES)[16,18–21] and theoretical band structure calculations,[22,23] no experimental study exists for the surface phonon dispersion curves. On the one hand, for van der Waals layered structures, often the dynamics of surface layers does not differ that much from the bulk and preliminary information can be extracted from experimental[24–26] and theoretical[27] bulk data. On the other hand, the presence of topological surface electronic states at the Fermi level promises peculiar effects on the surface.[28–30] So far information about the surface phonon dispersion curves of Sb_2Te_3(111) was limited to *ab initio* calculations using density functional perturbation theory (DFPT).[30] In this work we determine the surface phonon dispersion and discuss several additional inelastic events in atom-surface scattering such as kinematical focusing, resonance enhancement and surfing. Using the time-of-flight (TOF) technique[31] we determine the surface phonon dispersion in the energy

[a] *Institute of Experimental Physics, Graz University of Technology, 8010 Graz, Austria. E-mail: ruckhofer@tugraz.at*
[b] *Department of Physics and Astronomy, Interdisciplinary Nanoscience Center (iNANO), Aarhus University, 8000 Aarhus, Denmark*
[c] *Center for Materials Crystallography, Department of Chemistry and iNANO, Aarhus University, 8000 Aarhus, Denmark*
[d] *Dipartimento di Scienza dei Materiali, Universitá degli Studi di Milano-Bicocca, Milano, Italy*
[e] *Donostia International Physics Center (DIPC) and University of the Basque Country, 20018 Donostia/San Sebastian, Spain*

region below 11 meV based on helium atom scattering (HAS) and compare the results with existing *ab initio* calculations. HAS with incident energies in the low meV range has been widely used to probe low-energy surface excitations with the best available resolution, while being an inert completely non destructive technique.[31,32]

2 Experimental details and sample characterisation

The reported measurements were performed on a HAS apparatus which generates a nearly monochromatic beam ($\Delta E/E \approx 2\%$) of ^{4}He that is scattered off the sample surface in a fixed 91.5° source-sample-detector geometry. The beam is produced in a supersonic expansion of He through a 10 μm nozzle followed by extracting the core of the supersonic expansion via a 310 μm skimmer. For a detailed description of the apparatus refer to ref. 33.

The analysis of the inelastically scattered He atoms allows to determine the surface phonon branches in the acoustic and optical regions. The impinging He atoms with energies in the low meV range are exclusively scattered by the surface charge density.[34,35] Inelastic scattering from surface phonons occurs via the phonon-induced charge density oscillations, which can be used for the determination of the electron–phonon (e–ph) interaction constant.[36,37] Antimony telluride has a rhombohedral crystal structure consisting of five atomic layers, arranged along the *z*-direction (perpendicular to the surface), known as quintuple layers (QLs) as seen in Fig. 1c.[38] Each QL consists of two equivalent tellurium atoms, two equivalent antimony atoms and a third tellurium atom. The bonding is strong between the atomic layers within a QL but much weaker, predominantly of the van der Waals type, between two QLs. When cleaved along the (111) plane the upper-most atomic layer consists of tellurium, followed by an antimony layer below and so forth.

The investigated crystal was formed by slowly cooling the melt in a quartz tube similar to the procedure described in ref. 39 and 40 and the phase purity of the synthesised sample was measured by X-ray diffraction. The unit cell parameters were extracted based on a Rietveld refinement. Afterwards the crystal rod was cleaved along the (111) plane and for the measurements a small sample was attached onto a sample plate with electrically and thermally conductive epoxy. The surface electronic structure of the samples was characterised by ARPES at the SGM-3 beamline of ASTRID2.[41] The total energy and angular resolution were ≈30 meV and 0.1°, respectively. The sample temperature was ≈30 K and the photon energy was chosen to be 22 eV.

Previously to the HAS measurements, in order to obtain a clean surface, the sample was cleaved *in situ* under high vacuum conditions in a separate load lock chamber,[42] before storing the sample in the sample mount of the main chamber, to ensure minimal surface contamination. The sample can be heated using a button heater on the backside of the sample

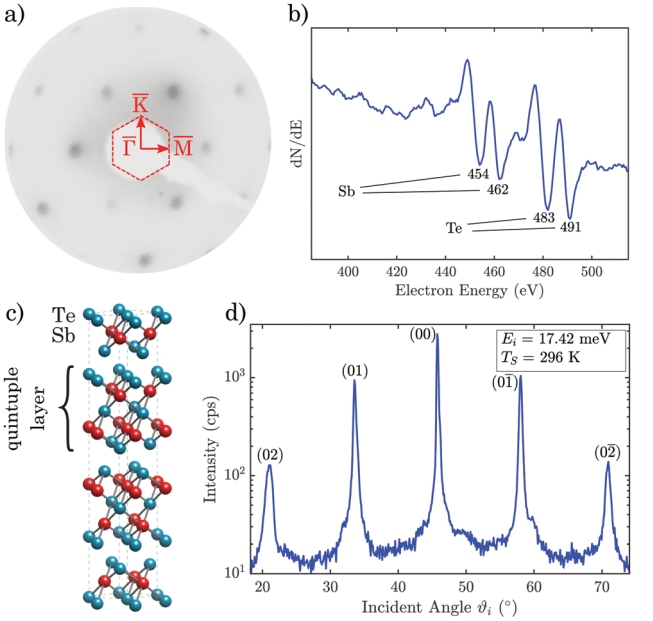

Fig. 1 (a) Represents the observed low energy electron diffraction pattern with the first Brillouin zone and the high symmetry directions $\overline{\Gamma M}$ and $\overline{\Gamma K}$. In (b) the Auger spectrum of the investigated sample is depicted, indicating the characteristic peaks for the MN-transition of Te and Sb, while (c) shows the crystal structure of three quintuple layers of Sb_2Te_3 in the conventional hexagonal unit cell notation. A plot of the angular helium scattering distribution along the $\overline{\Gamma M}$ azimuth in (d) shows diffraction peaks up to second order.

mount or cooled down to 115 K via a thermal connection to a liquid nitrogen reservoir. Low energy electron diffraction was used for a first alignment of the sample along the high symmetry orientation (Fig. 1a). Additionally, before running scattering experiments, the composition of the sample was analysed by Auger electron spectroscopy. The obtained spectrum can be seen in Fig. 1b, which shows significant intensities at the expected energies for single-elemental antimony and tellurium, when compared to spectra from literature.[43]

The angular HAS distribution along the $\overline{\Gamma M}$ azimuth in Fig. 1d shows diffraction peaks up to second order. The scattered intensity is plotted on a logarithmic scale with an incident energy of E_i = 17.4 meV and the sample held at room temperature. The high signal-to-noise ratio and the small full width at half maximum of the specular peak are an indication of the good crystal quality after cleaving. The high intensity of the diffraction peaks suggests a large surface electronic corrugation (Sb_2Te_3(111) exhibits a surface electronic corrugation of 6.6% of the lattice constant[44]) which is a necessary ingredient for various phenomena, *e.g.* involving bound state resonances.

Energy dispersive spectra for inelastic scattering were performed using TOF measurements with a pseudo-random chopper disc. After deconvolution with the pseudo-random chopper sequence, the TOF signal is further transformed to an energy transfer scale which allows to determine inelastic (phonon) scattering events.[33] The scattering spectra were mainly taken with the crystal at room temperature, while a few spectra were taken with the sample cooled down to 115 K and the incident He beam energy was varied between 10 and 18 meV.

3 Results and discussion

Details of the phonon dispersion are closely linked to the electronic structure and screening of a system and this is particularly relevant for the surface phonon dispersion of topological insulators where the surface electronic properties are drastically different from those of the bulk. It is therefore important to characterise the crystals in terms of their bulk doping in order to identify the Fermi surface elements that can contribute to screening. For Sb_2Te_3 the as-grown crystals are typically strongly p-doped, up to a degree where the valence band maximum at $\bar{\Gamma}$ and a hole pocket along the $\overline{\Gamma M}$ direction can contribute to the surface Fermi surface.[19,20,30] The latter is confirmed in ARPES measurements of the current sample as described in the following.

3.1 Surface electronic structure

The photoemission intensity at the Fermi energy is given in Fig. 2a, showing a flower-like pattern. The closed contour around $\bar{\Gamma}$ and the petals of the flower have both the character of hole pockets, as can be seen from the detailed dispersion in Fig. 2b.

Indeed, it is seen that the state near $\bar{\Gamma}$ results from both the valence band maximum, leading to the blurred intensity near the Fermi level at $k_{\parallel} \approx 0$, and the lower part of the topological surface state dispersion that gives rise to a somewhat sharper linear feature, marked by an arrow in the figure. The band forming the hole pocket (flower petal) along $\overline{\Gamma M}$ is seen as a diffuse intensity in an energy interval between $\approx$0.3 eV and the Fermi energy. Note that the observation of broad bands from bulk states is common in ARPES and related to the $k_{\perp}$ smearing that results from the short inelastic mean free path of the photoelectrons. The conclusion from the ARPES characterisation is that the sample is indeed strongly p-doped, giving rise to two different types of (bulk) hole pockets.

3.2 Surface phonon dispersion

The surface phonon events were determined from a multitude of TOF spectra at various incident energies E_i and incident angles ϑ_i to fully cover the Brillouin zone along both high symmetry directions (see Appendix A for various TOF spectra).

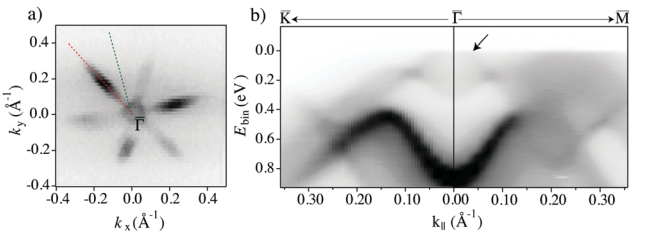

Fig. 2 (a) Photoemission intensity at the Fermi level with dark corresponding to high intensity. Red and green dashed lines indicate the $\overline{\Gamma M}$ and $\overline{\Gamma K}$ directions in the surface Brillouin zone, respectively. (b) Photoemission intensity along $\overline{K\Gamma M}$ as a function of binding energy E_{bin}, illustrating the character of the features that give rise to the Fermi surface. The arrow marks the location of the topological surface state.

The peaks in the energy domain of the TOF spectra were transformed to the wavevector domain using the so called scancurve (SC). The SC links all accessible energy transfers to the corresponding parallel momentum transfer during an inelastic event and is given by

$$k_i \sin\vartheta_i + Q = \sin\vartheta_f \sqrt{2m(E_i + E_{ph})/\hbar} \quad (1)$$

with k_i being the incident wavevector, $\sin\vartheta_{i,f}$ the incident and final scattering angle, Q the wavevector, m the He atom mass and E_{ph} the phonon energy. For a more detailed description of the determination of the phonon energies see ref. 29 and 45.

As shown by D. Campi *et al.*,[30] the inclusion of spin–orbit coupling (SOC) in *ab initio* calculations of the surface phonon dispersion has negligible effects. Hence, the reported surface phonon dispersion curves based on DFPT calculations (without SOC) for a slab consisting of three QLs are reproduced in Fig. 3 as solid grey lines. The experimentally obtained surface phonon energies are plotted as symbols on top of the theoretical calculations in Fig. 3.

We are able to resolve surface phonon events with energies up to 11 meV along both high symmetry directions. Each phonon event has been marked with a mode related colour and tag, according to its vicinity to the calculated modes. Due to many avoided crossings an accurate assignment of the optical modes becomes more difficult. In general the experimental surface phonon dispersion is in good agreement with the DFPT calculations except for the low energy modes (1–4 meV) marked as green diamonds which will be discussed below (Section 3.4).

According to the DFPT calculations, there are altogether 45 phonon branches (of which only the lower 24 are displayed as solid grey lines in Fig. 3), organised into 15 bands associated

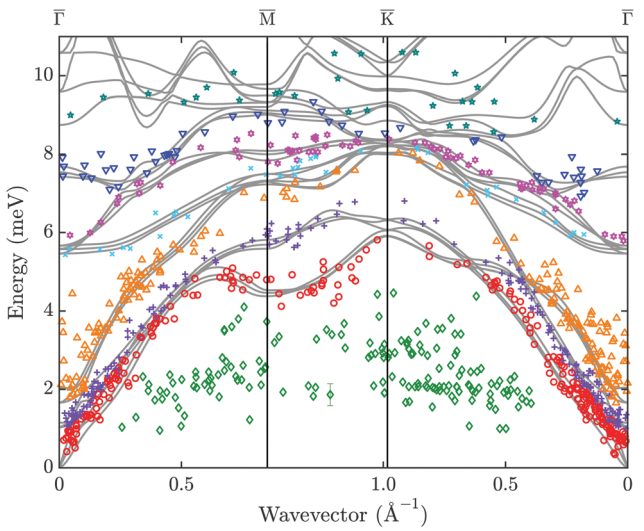

Fig. 3 Experimental surface phonon dispersion of Sb_2Te_3(111) from helium atom scattering (symbols) in comparison with DFPT calculations for three quintuple layers in the lower part of the phonon spectrum (solid grey lines).[30] The assignment of the data points (colour and tag) to different modes is based on the proximity to the theoretical modes. One exemplary error bar is shown at an energy of $\approx$2 meV.

with the 15 degrees of freedom of Sb_2Te_3. Besides the 3 acoustic modes, there are two low-energy bands (<2 meV at $\bar{\Gamma}$) where in each QL the central Te layer is at rest and the two external bilayers move rigidly and symmetrically normal ($A_g(1)$) or parallel ($E_g(1)$) to the slab.[27]

The corresponding experimentally obtained acoustic branches are shown as red circles, purple crosses and orange triangles in Fig. 3, with the red circles being the Rayleigh wave (RW), starting with zero energy at the $\bar{\Gamma}$ point. In general, a high concentration of experimental data points is found in the acoustic region, including the Rayleigh mode. Inelastic events from the RW give the highest intensity in the respective TOF spectra, confirming the high intensity of the RW as also found for other binary TIs such as Bi_2Se_3 and Bi_2Te_3, respectively.[28,29] Note that in contrast to the recent report of two RWs in Bi_2Te_3[46] there exists only one RW, either as a surface-localised wave or as an in-band resonance (pseudo-surface wave), as a result of continuum theory.[28,29,32]

3.3 Phonon group velocity

As mentioned above, the energetically lowest mode in the surface phonon dispersion is the RW. Its band starts at zero energy at the $\bar{\Gamma}$-point of the surface Brillouin zone with a linear dispersion in the long wavelength ($Q \to 0$) limit.

The group velocity of the RW can be determined from the slope of its dispersion curve at small wavevectors. Therefore, the measured data points are fitted with a linear relation in the low energy range assuming an intercept with the $\bar{\Gamma}$-point at $Q = 0$. Due to the fact, that for Sb_2Te_3 the RW and the second acoustic mode proceed parallel and rather close to each other, the assignment of measured points is not always unambiguous, which leads to a rather high uncertainty for the determined slopes along $\overline{\Gamma M}$ and $\overline{\Gamma K}$ in Table 1.

By means of the elastic constants of Sb_2Te_3 calculated *ab initio* by Lu *et al.*,[47] and a crystal density of 6.488 g cm^{-3},[48] the bulk transverse speed of sound along $\overline{\Gamma K}$ can be calculated[49] and is found to be 1620 m s^{-1}. As seen in Table 1, the group velocity of the RW along this direction is only slightly less than the bulk transverse acoustic speed of sound with a difference that is, however, much smaller than the experimental uncertainty.

3.4 Low energy modes

When looking at Fig. 3 it becomes evident that several peaks at energies between 1–4 meV are not reproduced in the DFPT calculations. These events cannot be assigned to any surface phonon mode and need further discussion. One could possibly ascribe two separate branches with a dispersion to the plotted data points, though with some difficulty given the number of data points and their spread.

Table 1 Slopes of the RW along the $\overline{\Gamma M}$ and $\overline{\Gamma K}$ direction based on a linear fit and the corresponding group velocities v_{RW} of the RW

	Slope (meV Å)	v_{RW} (m s^{-1})
$\overline{\Gamma M}$	10.9 ± 1.0	1650 ± 160
$\overline{\Gamma K}$	10.0 ± 0.5	1590 ± 80

Similar low-energy excitations observed with HAS in the gap below the RW branch have been reported previously in two other topological materials, Sb(111)[50] and Bi_2Se_3(111).[29] In both cases they could be assigned to low-energy surface electron collective excitations, namely phasons and amplitons, associated with a charge density wave (CDW) induced by e–ph interaction. In Sb(111) a quasi-commensurate CDW originates from the Kelly–Falicov multivalley e–ph coupling connecting $\bar{M}$-point electron pockets,[50] while in Bi_2Se_3(111) a long-period CDW has been associated with e–ph coupling connecting surface quantum-well states.[29] In both cases distinct CDW features are observed at low temperature in the HAS diffraction spectra, though under bound-state resonance enhancement conditions in Bi_2Se_3(111).

Although the similarities of present low-energy data with those observed in Sb(111) and Bi_2Se_3(111) are quite evident, low-lying frustrated translational modes of adsorbates can be another possible source of these data points.[51] This possibility is however rather remote in view of the good quality of the surface during experiments, as witnessed by the comparatively low intensity of the diffuse elastic peak in the TOF spectra (see, *e.g.* Fig. 4a)

Hence we conclude that the two branches are likely to be caused by phasons/amplitons in analogy to the observations made on Sb(111) and Bi_2Se_3(111), although a more thorough investigation is needed in order to unambiguously assign and understand these excitations.

3.5 Resonance enhancement

The intensity of a specific phonon event might be increased if a bound state resonance is involved – therefore termed resonance enhancement. A He atom might go into a final state which is a bound state of energy $-|\varepsilon_n| + \hbar^2 K_f^2/2m^*$, with K_f being the final parallel vector and m^* the effective mass of the atom in the bound state.[51] Based on the conservation of energy and parallel momentum, the corresponding equation for inelastic selective adsorption is[51]

$$\hbar\omega(Q) = E_i + |\varepsilon_n| - \frac{\hbar^2}{2m}\left[(k_i \sin\vartheta_i - G_{||} - Q)^2 + G_\perp{}^2\right], \qquad (2)$$

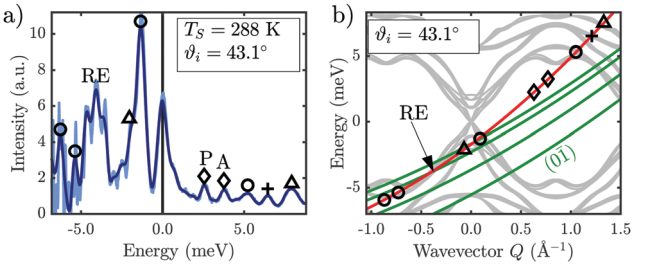

Fig. 4 (a) shows a TOF-spectrum at ϑ_i = 43.1° with the sample at room temperature, exhibiting phonon processes and low energy excitations as well as a resonance-enhanced phonon process. The light blue line depicts the raw data after conversion to an energy transfer scale while the dark blue line shows the signal after binning based on constant energy bins (see Appendix). In (b) the resonance conditions (eqn (2)) for the $(0\bar{1})$ **G**-vector together with the scancurve are drawn on top of the DFPT calculations (grey lines). The symbols correspond to the phonon events of the TOF spectrum to the left.

with $G_\parallel$ and $G_\perp$ being the parallel and perpendicular components of the **G**-vector, respectively.

If the resonance condition (2) intersects with the SC (1) at a specific phonon branch, the intensity of this particular phonon will be enhanced in the TOF spectrum. Based on the bound states ε_n for Sb_2Te_3 (ε_0 = 4.27 meV, ε_1 = 2.37 meV, ε_2 = 0.9 meV, ε_3 = 0.4 meV),[44] the condition is fulfilled in Fig. 4b, where the bound state ε_2 of the resonance curve with an interacting **G**-vector $(0\bar{1})$ intersects the SC at an energy of −4 meV. The intensity of this created phonon is greatly enhanced in the TOF spectrum (Fig. 4a), when compared to measurements which do not satisfy the condition. Recent work showed that these resonance enhancing effects can in turn be used to observe low-energy surface electron collective excitations.[29]

3.6 Kinematical focusing, focussed inelastic resonance and surfing

In addition to phonon resonance enhancement a variety of other resonance and focusing phenomena can arise upon scattering from a corrugated surface,[51] as listed below. These processes can be described by looking at the equations for the SC and the resonance conditions as well as the lowest modes of the surface phonon dispersion. The upper left graph of Fig. 5 shows an angular scan where the incident angle ϑ_i is varied along the $\overline{\Gamma M}$ azimuth with the sample at a temperature of 113 K. Upon enlarging the *y*-scale compared to Fig. 1d, additional peaks and dips appear in the diffuse inelastic background. Below the measured curve the bound state resonances for the four known bound states[44] are depicted. The different colours correspond to the different interacting reciprocal lattice vectors.

The three scattering phenomena kinematical focusing (i), surfing (ii) and resonance enhancement (iii) are plotted in the lower panels of Fig. 5 as energy $\hbar\omega(Q)$ versus wavevector Q. Here we use the convention that the forward creation process is displayed in the third quadrant ($Q < 0$, $\hbar\omega(Q) < 0$) as frequently used in HAS analysis.[29,52] Therefore positive energies in Fig. 5 correspond to annihilation and backward propagation. The purely inelastic process occurs when the SC intersects with a branch in the phonon dispersion and can be measured with the TOF technique described above.

(i) An effect known as kinematical focusing[53] (KF) might show up at a specific incident angle ϑ_i and incident energy E_i when the SC lies tangent to a phonon branch. KF gives rise to a saw-tooth peak in the angular scattering distribution due to the increased inelastic background in the elastic signal. The characteristic peak shape can clearly be identified in the angular scan (upper left panel of Fig. 5) at $\vartheta_i = 32^\circ$ and $\vartheta_i = 43^\circ$. For the first angle the corresponding SC is plotted in red in Fig. 5i together with the two lowest modes of the calculated phonon dispersion. The point of tangency is marked with KF and can be observed in the angular distribution as well as in the corresponding TOF spectrum.

(ii) We now turn to the effect of surfing, which occurs when a resonance curve lies tangent to a surface phonon branch. In

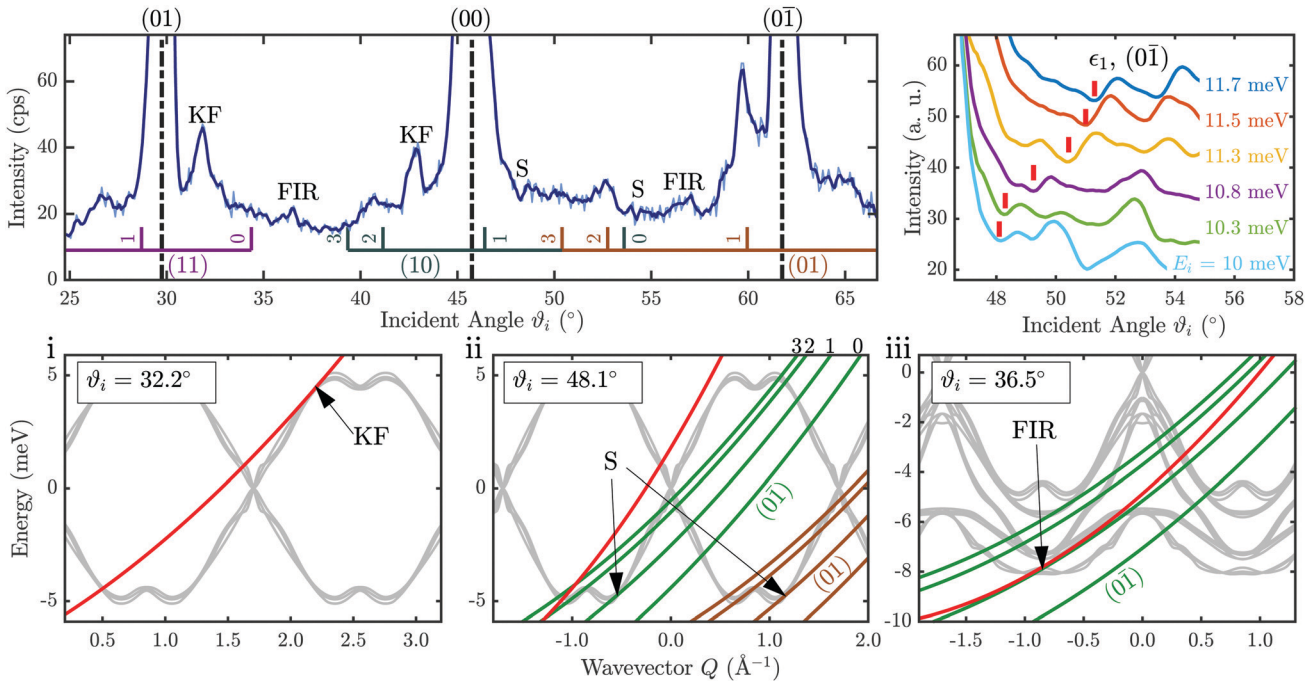

Fig. 5 Diagrams illustrating various HAS focusing effects as a function of parallel momentum (wavevector) Q, for an incident energy E_i = 10.3 meV. Top left panel: Angular scan along the $\overline{\Gamma M}$ azimuth at a surface temperature T_s = 113 K (light blue line: raw data, dark blue line: smoothed data). The lines below the measured curve indicate selective adsorption resonance processes with the colours corresponding to different interacting **G**-vectors. Top right: Tracking of the surfing feature (highlighted by the red bar) with increasing incident beam energy E_i. The lower panels show (from left to right) the effects kinematical focusing (KF), surfing (S) and focused inelastic resonance (FIR). The red curves depict the scancurve while the green curves show the resonance conditions (eqn (2)) with the corresponding **G**-vector.

this case, the impinging He atom is selectively adsorbed into a bound state ε_n with the aid of a surface phonon. In comparison to the "ordinary" elastic selective adsorption this process can occur even without the exchange of a reciprocal lattice vector. The tangency condition yields a concentration of beams inelastically scattered into the given bound state and therefore a dip in the final beam around a special incident angle. Using the bound state energy values for Sb_2Te_3[44] a set of resonance curves are plotted as green lines in Fig. 5ii. The tangency of one of these curves with a phonon branch gives rise to a dip in the angular distribution. If this special condition is fulfilled the atom and the phonon wave exhibit the same velocity on the surface and travel together, hence the effect is called surfing. According to ref. 51 the atom stays on the surface for a longer time during surfing compared to the lifetime of the He atom in a bound state.[44] However, based on the signal-to-noise ratio of our data it is difficult to extract an actual linewidth and thus the corresponding lifetime. Hence we cannot conclude on any values for the lifetime.

In Fig. 5ii the surfing effect is shown for an incident angle of $\vartheta_i = 57.1^\circ$, where the resonance curves of the bound state ε_1 for the **G**-vectors $(0\bar{1})$ and (01) are tangent to the acoustic phonon branch. In the angular spectrum the surfing conditions at various angles are indicated with an S, yielding a dip in the scattered intensity. To further support the finding of the surfing feature the dip can be monitored in dependence of the incident energy E_i. In the top right panel of Fig. 5 the surfing dip is shown for incident energies between $E_i = 10.7$ and 11.7 meV. The angular spectra were smoothed using a Savitzky–Golay filter and the red bars mark sequences of features assigned to the $(0\bar{1})$ surfing condition including the ε_1 bound state.

(iii) Finally we discuss the effect of focussed inelastic resonance (FIR), which occurs when the SC (1) is tangent to a resonance curve (2) within an energy region where surface phonons are expected.[32,54] When combining these two equations the expected FIR position is given by

$$\tan^2 \vartheta_f^{FIR} = \left[\frac{2m}{\hbar^2}|\varepsilon_n| - \mathbf{G}^2\right]\frac{1}{G_\parallel{}^2}. \quad (3)$$

Hence the incident angle ϑ_i for a FIR follows from the fixed source-detector geometry ($\vartheta_i + \vartheta_f = \vartheta_{SD}$). A very characteristic property of a FIR is the independence of (3) with respect to the incident energy.

In the angular scan of Fig. 5 two FIR features are present at $\vartheta_i = 36.5^\circ$ and $\vartheta_i = 56.4^\circ$ yielding an increased scattered intensity. A comparison with angular scans at similar incident energies shows that the FIR peaks are still present at the same incident angle as expected, according to (3). In the lower right most plot of Fig. 5 ($\vartheta_i = 36.5$) the resonance curve becomes tangent to the SC for an optical phonon branch at around 8 meV.

Following this systematic approach we are able to interpret all significant peaks of the angular scan in Fig. 5 using the effects described above. All peaks which are not labelled are attributed to selective adsorption resonances indicated by the vertical coloured lines below the measured data.

4 Conclusions

In summary, we have investigated various inelastic interactions of helium with Sb_2Te_3 which are experimentally detected in TOF spectra as well as in angular scans. A multitude of TOF spectra was used to determine the surface phonon dispersion for the $\overline{\Gamma M}$ and $\overline{\Gamma KM}$ directions. A comparison with theoretical calculations based on density functional perturbation theory shows good agreement with the experimental data. Similar to earlier works, the strongest phonon intensities originate from the Rayleigh mode. From the slope of the Rayleigh mode the phonon group velocity is determined to be $v_R \approx 1600$ m s^{-1}. In addition to phonon creation and annihilation processes, we observe further peculiar inelastic events below the Rayleigh mode. In view of similar observations made on the topological materials Sb(111) and Bi_2Se_3(111), they are tentatively assigned to the dispersion curves of phasons and amplitons associated with a charge density wave.

Furthermore, a systematic analysis of angular diffraction scans shows that several additional inelastic scattering events are observable for He atom scattering from Sb_2Te_3. These include resonance enhancement, kinematical focusing, focused inelastic resonances and surfing.

Conflicts of interest

There are no conflicts to declare.

A Additional TOF spectra

For the determination of the surface phonon dispersion (Fig. 3) a multitude of TOF spectra were measured with different incident energies E_i and incident angles ϑ_i. In Fig. 6 three exemplary TOF spectra are shown in the $\overline{\Gamma M}$ direction, after conversion to an energy transfer scale. Negative energy transfer corresponds to phonon creation, while positive energy transfer corresponds to phonon annihilation.

Because of the non-linearity introduced by the conversion from the flight time to the energy transfer scale, the data has to be multiplied with the corresponding Jacobian in order to preserve the intensity. Due to the process, experimental noise increases on the creation side ($\Delta E = E_f - E_i < 0$) as seen in the light blue line in Fig. 6. The latter makes it difficult to distinguish peaks in the (far) creation side and therefore, the (non-linear) energy scale is usually divided in equally spaced energy bins over which the signal is averaged.[55] The dark blue line shows the signal after binning, resulting in a smoother line.

The peaks in Fig. 6 identified as phonon events are indicated with different symbols, which attribute the peaks to the specific phonon branches (same symbols as in Fig. 3). The symbols are drawn on the SC (1) plotted as a dashed orange line, relating the energy transfer of a phonon event to the momentum transfer ΔK (right ordinate in Fig. 6).

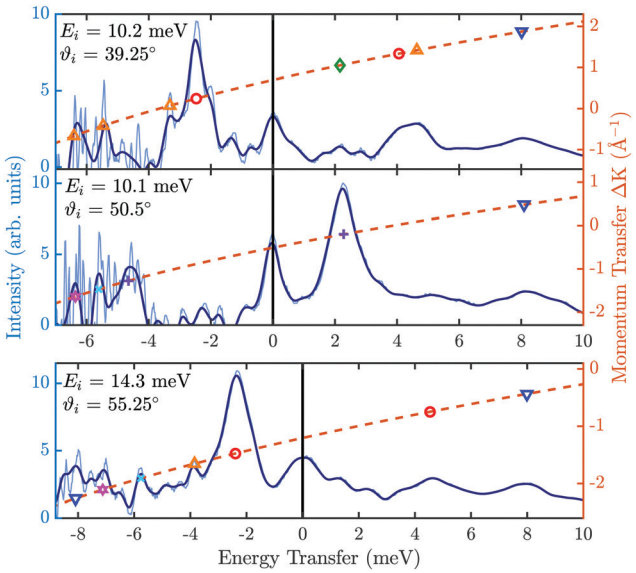

Fig. 6 Compilation of several TOF spectra measured along the $\overline{\Gamma M}$ azimuth at various incident energies E_i and angles ϑ_i. For the two upper graphs the temperature of the He nozzle was set to 50 K and for the bottom one to 65 K. All shown scans were taken with the sample at room temperature. The light blue line shows the signal after conversion to the energy transfer scale while the dark blue line is the result of averaging based on constant energy bins (see text). The vertical black line illustrates diffuse elastic scattering while the dashed orange line is the scan curve (1) (*y*-axis on the right-handside), relating energy transfer to momentum transfer. The symbols denote peaks in the TOF spectrum which have been assigned to phonon events.

Acknowledgements

We would like to thank D. Campi for many helpful discussions and the *ab initio* surface phonon dispersion curves from ref. 30. The authors are grateful for financial support by the FWF (Austrian Science Fund) within the project P29641-N36, as well as by NAWI Graz. We would like to thank the Aarhus University Research Foundation, VILLUM FOUNDATION *via* the Centre of Excellence for Dirac Materials (Grant No. 11744) and the SPP1666 of the DFG (Grant No. HO 5150/1-2) for financial support. M. Bremholm acknowledges financial support from the Center of Materials Crystallography (CMC) and the Danish National Research Foundation (DNRF93).

References

1 G. J. Snyder and E. S. Toberer, *Nat. Mater.*, 2008, **7**, 105–114.
2 M. Wuttig and N. Yamada, *Nat. Mater.*, 2007, **6**, 824–832.
3 L. D. Hicks and M. S. Dresselhaus, *MRS Proc.*, 1993, **326**, 413.
4 S. Zastrow, J. Gooth, T. Boehnert, S. Heiderich, W. Toellner, S. Heimann, S. Schulz and K. Nielsch, *Semicond. Sci. Technol.*, 2013, **28**, 035010.
5 Z. Zhang, H. Zhang, Y. Wu, Z. Zeng and Z. Hu, *Appl. Phys. A: Mater. Sci. Process.*, 2015, **118**, 1043–1051.
6 N. F. Hinsche, S. Zastrow, J. Gooth, L. Pudewill, R. Zierold, F. Rittweger, T. Rauch, J. Henk, K. Nielsch and I. Mertig, *ACS Nano*, 2015, **9**, 4406–4411.
7 S. Fujimori, S. Yagi, H. Yamazaki and N. Funakoshi, *J. Appl. Phys.*, 1988, **64**, 1000–1004.
8 H. Zhang, C.-X. Liu, X.-L. Qi, X. Dai, Z. Fang and S.-C. Zhang, *Nat. Phys.*, 2009, **5**, 438.
9 J. Zhang, C.-Z. Chang, Z. Zhang, J. Wen, X. Feng, K. Li, M. Liu, K. He, L. Wang, X. Chen, Q.-K. Xue, X. Ma and Y. Wang, *Nat. Commun.*, 2011, **2**, 574.
10 P. Sessi, O. Storz, T. Bathon, S. Wilfert, K. A. Kokh, O. E. Tereshchenko, G. Bihlmayer and M. Bode, *Phys. Rev. B*, 2016, **93**, 035110.
11 O. A. Pankratov, S. V. Pakhomov and B. A. Volkov, *Solid State Commun.*, 1987, **61**, 93–96.
12 C. Wu, B. A. Bernevig and S.-C. Zhang, *Phys. Rev. Lett.*, 2006, **96**, 106401.
13 L. Fu, C. L. Kane and E. J. Mele, *Phys. Rev. Lett.*, 2007, **98**, 106803.
14 X.-L. Qi and S.-C. Zhang, *Phys. Today*, 2010, **63**, 33–38.
15 C. Pauly, G. Bihlmayer, M. Liebmann, M. Grob, A. Georgi, D. Subramaniam, M. R. Scholz, J. Sánchez-Barriga, A. Varykhalov, S. Blügel, O. Rader and M. Morgenstern, *Phys. Rev. B: Condens. Matter Mater. Phys.*, 2012, **86**, 235106.
16 L. Plucinski, A. Herdt, S. Fahrendorf, G. Bihlmayer, G. Mussler, S. Döring, J. Kampmeier, F. Matthes, D. E. Bürgler, D. Grützmacher, S. Blügel and C. M. Schneider, *J. Appl. Phys.*, 2013, **113**, 053706.
17 G. Wang, X. Zhu, J. Wen, X. Chen, K. He, L. Wang, X. Ma, Y. Liu, X. Dai, Z. Fang, J. Jia and Q. Xue, *Nano Res.*, 2010, **3**, 874–880.
18 C. Seibel, H. Maaß, M. Ohtaka, S. Fiedler, C. Jünger, C.-H. Min, H. Bentmann, K. Sakamoto and F. Reinert, *Phys. Rev. B: Condens. Matter Mater. Phys.*, 2012, **86**, 161105.
19 J. Reimann, J. Güdde, K. Kuroda, E. V. Chulkov and U. Höfer, *Phys. Rev. B: Condens. Matter Mater. Phys.*, 2014, **90**, 081106.
20 S. Zhu, Y. Ishida, K. Kuroda, K. Sumida, M. Ye, J. Wang, H. Pan, M. Taniguchi, S. Qiao, S. Shin and A. Kimura, *Sci. Rep.*, 2015, **5**, 13213.
21 Y. C. Arango, L. Huang, C. Chen, J. Avila, M. C. Asensio, D. Grützmacher, H. Lüth, J. G. Lu and T. Schäpers, *Sci. Rep.*, 2016, **6**, 29493.
22 B. Y. Yavorsky, N. F. Hinsche, I. Mertig and P. Zahn, *Phys. Rev. B: Condens. Matter Mater. Phys.*, 2011, **84**, 165208.
23 I. A. Nechaev, I. Aguilera, V. De Renzi, A. di Bona, A. Lodi Rizzini, A. M. Mio, G. Nicotra, A. Politano, S. Scalese, Z. S. Aliev, M. B. Babanly, C. Friedrich, S. Blügel and E. V. Chulkov, *Phys. Rev. B: Condens. Matter Mater. Phys.*, 2015, **91**, 245123.
24 W. Richter and C. R. Becker, *Phys. Status Solidi B*, 1977, **84**, 619–628.
25 Y. Kim, X. Chen, Z. Wang, J. Shi, I. Miotkowski, Y. P. Chen, P. A. Sharma, A. L. Lima Sharma, M. A. Hekmaty, Z. Jiang and D. Smirnov, *Appl. Phys. Lett.*, 2012, **100**, 071907.
26 V. Bragaglia, M. Ramsteiner, D. Schick, J. E. Boschker, R. Mitzner, R. Calarco and K. Holldack, *Sci. Rep.*, 2020, **10**, 12962.
27 G. C. Sosso, S. Caravati and M. Bernasconi, *J. Phys.: Condens. Matter*, 2009, **21**, 095410.

28 A. Tamtögl, D. Campi, M. Bremholm, E. M. J. Hedegaard, B. B. Iversen, M. Bianchi, P. Hofmann, N. Marzari, G. Benedek, J. Ellis and W. Allison, *Nanoscale*, 2018, **10**, 14627–14636.
29 A. Ruckhofer, D. Campi, M. Bremholm, P. Hofmann, G. Benedek, M. Bernasconi, W. E. Ernst and A. Tamtögl, *Phys. Rev. Res.*, 2020, **2**, 023186.
30 D. Campi, M. Bernasconi and G. Benedek, *Surf. Sci.*, 2018, **678**, 46–51.
31 D. Farias and K.-H. Rieder, *Rep. Prog. Phys.*, 1998, **61**, 1575–1664.
32 G. Benedek and J. P. Toennies, *Atomic Scale Dynamics at Surfaces*, Springer Berlin Heidelberg, 2018.
33 A. Tamtögl, M. Mayrhofer-Reinhartshuber, N. Balak, W. E. Ernst and K. H. Rieder, *J. Phys.: Condens. Matter*, 2010, **22**, 304019.
34 A. Tamtögl, M. Mayrhofer-Reinhartshuber, P. Kraus and W. E. Ernst, *Surf. Sci.*, 2013, **617**, 225–228.
35 A. Tamtögl, P. Kraus, M. Mayrhofer-Reinhartshuber, D. Campi, M. Bernasconi, G. Benedek and W. E. Ernst, *Phys. Rev. B: Condens. Matter Mater. Phys.*, 2013, **87**, 035410.
36 G. Benedek, S. Miret-Artés, J. R. Manson, A. Ruckhofer, W. E. Ernst and A. Tamtögl, *J. Phys. Chem. Lett.*, 2020, 1927–1933.
37 G. Benedek, J. R. Manson and S. Miret-Artés, *Adv. Mater.*, 2020, **32**, 2002072.
38 X. Chen, H. D. Zhou, A. Kiswandhi, I. Miotkowski, Y. P. Chen, P. A. Sharma, A. L. Lima Sharma, M. A. Hekmaty, D. Smirnov and Z. Jiang, *Appl. Phys. Lett.*, 2011, **99**, 261912.
39 J.-L. Mi, M. Bremholm, M. Bianchi, K. Borup, S. Johnsen, M. Søndergaard, D. Guan, R. C. Hatch, P. Hofmann and B. B. Iversen, *Adv. Mater.*, 2013, **25**, 889–893.
40 M. Michiardi, I. Aguilera, M. Bianchi, V. E. de Carvalho, L. O. Ladeira, N. G. Teixeira, E. A. Soares, C. Friedrich, S. Blügel and P. Hofmann, *Phys. Rev. B: Condens. Matter Mater. Phys.*, 2014, **90**, 075105.
41 S. V. Hoffmann, C. Søndergaard, C. Schultz, Z. Li and P. Hofmann, *Nucl. Instrum. Methods Phys. Res., Sect. A*, 2004, **523**, 441.
42 A. Tamtögl, E. A. Carter, D. J. Ward, N. Avidor, P. R. Kole, A. P. Jardine, J. Ellis and W. Allison, *Rev. Sci. Instrum.*, 2016, **87**, 066108.
43 L. E. Davis, *Handbook of Auger Electron Spectroscopy: A Reference Book of Standard Data for Identification and Interpretation of Auger Electron Spectroscopy Data*, Physical Electronics, 1996.
44 A. Tamtögl, A. Ruckhofer, D. Campi, W. Allison and W. E. Ernst, *Phys. Chem. Chem. Phys.*, tbd, to be published.
45 J. P. Toennies, in *Surface Phonons*, ed. W. Kress and F. W. de Wette, Springer Berlin Heidelberg, Berlin, Heidelberg, 1991, pp. 111–166.
46 A. Trzaskowska and B. Mroz, *Sci. Rep.*, 2020, **10**, 11812.
47 Q. Lu, H.-Y. Zhang, Y. Cheng, X.-R. Chen and G.-F. Ji, *Chin. Phys. B*, 2016, **25**, 026401.
48 D. Bessas, I. Sergueev, H.-C. Wille, J. Perßon, D. Ebling and R. P. Hermann, *Phys. Rev. B: Condens. Matter Mater. Phys.*, 2012, **86**, 224301.
49 Y. C. Akgöz, G. A. Saunders and Z. Sümengen, *J. Mater. Sci.*, 1972, **7**, 279–288.
50 A. Tamtögl, P. Kraus, M. Mayrhofer-Reinhartshuber, G. Benedek, M. Bernasconi, D. Dragoni, D. Campi and W. E. Ernst, *npj Quantum Mater.*, 2019, **4**, 28.
51 G. Benedek, P. M. Echenique, J. P. Toennies and F. Traeger, *J. Phys.: Condens. Matter*, 2010, **22**, 304016.
52 G. Brusdeylins, R. B. Doak and J. P. Toennies, *Phys. Rev. B: Condens. Matter Mater. Phys.*, 1983, **27**, 3662–3685.
53 G. Benedek, G. Brusdeylins, J. P. Toennies and R. B. Doak, *Phys. Rev. B: Condens. Matter Mater. Phys.*, 1983, **27**, 2488–2493.
54 G. Benedek, R. Gerlach, A. Glebov, G. Lange, S. Miret-Artes, J. G. Skofronick and J. P. Toennies, *Phys. Rev. B: Condens. Matter Mater. Phys.*, 1996, **53**, 11211–11217.
55 P. Kraus, A. Tamtögl, M. Mayrhofer-Reinhartshuber, G. Benedek and W. E. Ernst, *Phys. Rev. B: Condens. Matter Mater. Phys.*, 2013, **87**, 245433.